

Extracting entanglement geometry from quantum states

Katharine Hyatt,¹ James R. Garrison,^{2,1} and Bela Bauer³

¹*Department of Physics, University of California, Santa Barbara, California 93106, USA*

²*Joint Quantum Institute and Joint Center for Quantum Information and Computer Science,
National Institute of Standards and Technology and University of Maryland, College Park, Maryland 20742, USA*

³*Station Q, Microsoft Research, Santa Barbara, California 93106, USA*

Tensor networks impose a notion of geometry on the entanglement of a quantum system. In some cases, this geometry is found to reproduce key properties of holographic dualities, and subsequently much work has focused on using tensor networks as tractable models for holographic dualities. Conventionally, the structure of the network – and hence the geometry – is largely fixed *a priori* by the choice of tensor network ansatz. Here, we evade this restriction and describe an unbiased approach that allows us to extract the appropriate geometry from a given quantum state. We develop an algorithm that iteratively finds a unitary circuit that transforms a given quantum state into an unentangled product state. We then analyze the structure of the resulting unitary circuits. In the case of non-interacting, critical systems in one dimension, we recover signatures of scale invariance in the unitary network, and we show that appropriately defined geodesic paths between physical degrees of freedom exhibit known properties of a hyperbolic geometry.

Tensor networks have proven to be a powerful and universal tool to describe quantum states. Originating as variational ansatz states for low-dimensional quantum systems, they have become a common language between condensed matter and quantum information theory. More recently, the realization that some key properties of holographic dualities [1–5] are reproduced in certain classes of tensor network states [6, 7] has led to new connections to quantum gravity. In particular, many questions about holographic dualities appear more tractable in tensor network models [8–18]. The study of the geometry of tensor network states underlies these developments. Here, the physical legs of the network represent the boundary of some emergent “holographic” space that is occupied by the tensor network. While in networks such as matrix-product states (MPS) [19–21] and projected entangled-pair states (PEPS) [22–24] this space just reflects the physical geometry, other networks – such as the multi-scale entanglement renormalization ansatz (MERA) [25, 26] – can have non-trivial geometry in this space [7]. We will refer to this geometry as “entanglement geometry”.

In this paper, we investigate whether this entanglement geometry can be extracted from a given quantum state without pre-imposing a particular structure on the tensor network [27]. We first describe a greedy, iterative algorithm that, given a quantum state, finds a 2-local unitary circuit that transforms this quantum state into an unentangled (product) state (see Fig. 1 for an illustration). Such unitary circuits, composed from unitary operators acting on two sites (which are not necessarily spatially close to each other), can be viewed as a particular class of tensor network states where the tensors are the unitary operators that form the circuit.

We then develop a framework for analyzing the geometry of these unitary circuits. First, we introduce a locally computable notion of distance between two points in the unitary circuit, thus inducing a geometry in the bulk. We then focus on a particular property of this ge-

ometry, namely the length of geodesics (shortest paths through the circuit) between physical (boundary) sites. A similar quantity has been previously discussed as a diagnostic of geometry in tensor networks [7], and reveals similar information as the minimal spanning surface in the celebrated Ryu-Takayanagi (RT) formula for the entanglement entropy in AdS/CFT [28, 29]. Crucially, our definition takes into account the strength of each local tensor, and thus allows us to numerically compute an appropriate length without imposing additional restrictions on the tensors [11] or *a priori* knowledge of the emergent geometry.

By applying these techniques to many-particle eigenstates of a model of non-interacting fermions in a disorder potential (which we can study for very large systems of up to hundreds of sites), we can observe regimes of both flat and hyperbolic emergent entanglement geometry and thus recover key aspects of the AdS/CFT duality [1–5]. Going beyond eigenstates, we study a quench from the localized to the delocalized regime, i.e. the evolution of a localized initial state under a Hamiltonian with vanishing disorder potential. In this case, the geodesics reveal detailed information about the deformation of the emergent geometry. The circuit progresses from a flat geometry to one where the geodesic length is independent of physical length: the emergent geometry becomes zero-dimensional. This process reproduces certain aspects of previous holographic analyses of quantum quenches [30–32].

In a complementary approach, we also examine the nature of emergent light cones in the unitary network. In the case of critical systems, these are found to exhibit features of scale invariance where each length scale of the system contributes equally to the bipartite entanglement of the system. Conversely, in the case of localized and thermal states, the light cones reveal that the entanglement is fully encoded in local and global operators, respectively. These results are discussed in App. A.

Disentangling algorithm— Our algorithm for finding a

unitary circuit – henceforth referred to as a *disentangling circuit* – is in many ways inspired by the strong-disorder renormalization group [33, 34]. However, there are two crucial differences. First, instead of acting on the Hamiltonian, the algorithm acts on a particular state. Second, rather than on the energetically strongest bond, at each step the algorithm works on the most strongly entangled pair of sites. The algorithm has two desirable properties. First, it works for a broad class of input states, including states that have area law and volume law entanglement. This comes at the cost of generating circuits that cannot in general be contracted in polynomial time. Second, each iteration of the iterative algorithm is completely determined by the output of the previous iteration; we thus avoid solving the challenging non-linear optimization problems that are usually encountered when optimizing a tensor network. Similar algorithms have been put forward in Refs. [17, 35].

We take as input a quantum state $|\psi\rangle$ on a lattice \mathcal{L} . We denote as ρ_{ij} the reduced density matrix on sites $i, j \in \mathcal{L}$, $\rho_{ij} = \text{Tr}_{\mathcal{L} \setminus \{i,j\}} |\psi\rangle\langle\psi|$, and as ρ_i the reduced density matrix on site i , $\rho_i = \text{Tr}_{\mathcal{L} \setminus \{i\}} |\psi\rangle\langle\psi|$, and $S(\rho) = -\text{Tr} \rho \log \rho$. The algorithm proceeds as follows:

Algorithm 1 (i) Calculate the mutual information between all pairs of sites, $I(i : j) = I(\rho_{ij}) \equiv S(\rho_i) + S(\rho_j) - S(\rho_{ij})$, and find the pair (i, j) with the largest mutual information. If all $I(i : j)$ are below some predefined threshold ϵ , terminate. (ii) Find the unitary matrix \hat{U}_{ij} that acts only on sites i and j and maximally reduces the amount of mutual information between these sites, i.e. solve $\min_{\hat{U}_{ij}} I(\hat{U}_{ij} \rho_{ij} \hat{U}_{ij}^\dagger)$. (iii) Set $|\psi\rangle \leftarrow \hat{U}_{ij} |\psi\rangle$, and return to step 1.

For details of the algorithm, including the method to find the optimal unitary for a lattice of qubits as well as for non-interacting fermions, we refer to App. B. For an exact representation of a many-body state in a Hilbert space of dimension $\dim \mathcal{H}$, one iteration of the above algorithm can be carried out with computational cost $\mathcal{O}(L \dim \mathcal{H})$ [36]. For a system of non-interacting fermions, however, the algorithm can be completely expressed in terms of the correlation matrix $C_{ij} = \langle \hat{c}_i^\dagger \hat{c}_j \rangle$ [37–39], as discussed in detail in App. B. Given the initial correlation matrix, the algorithm can be performed in $\mathcal{O}(L)$ operations per iteration, where L is the number of fermionic modes. In all cases, a single iteration of the algorithm can be performed as fast or faster than finding the eigenstates.

The algorithm ultimately constructs a unitary circuit $\hat{U} = \hat{U}_{i_\tau j_\tau}^{(\tau)} \dots \hat{U}_{i_2 j_2}^{(2)} \hat{U}_{i_1 j_1}^{(1)}$ acting on the initial state $|\Psi\rangle$, where $\hat{U}_{i_\tau j_\tau}^{(\tau)}$ is the unitary obtained in the τ 'th step. The number of steps the algorithm executes corresponds to the depth of the circuit. The circuit is 2-local in the sense that each unitary acts on two sites, but it is *not* local in the geometry of the lattice because the two sites i and j are allowed to be arbitrarily far apart. Furthermore, this circuit is not unique: an ambiguity arises since the unitary can always be followed by a swap

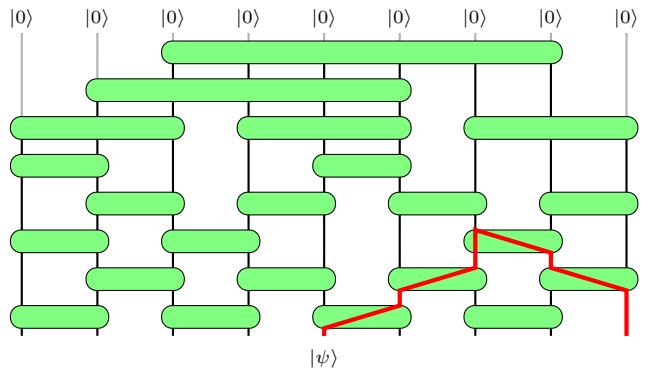


FIG. 1. Example of a two-local unitary network, where each tensor acts only on the two qubits that are at its ends. The thick red line indicates a geodesic between the 5th and 9th qubit (from the left), following a path through the circuit as given by Fig. 2.

of the two sites or a single-site unitary while keeping the mutual information the same. In order to partially lift this ambiguity, we choose the unitary to minimize the entangling power $P(\hat{U})$. To define the entangling power of a two-site unitary \hat{U}_{ij} , consider its decomposition $\hat{U}_{ij} = \sum_{\alpha} \sqrt{\lambda_{\alpha}} \hat{X}_i^{\alpha} \otimes \hat{Y}_j^{\alpha}$, where \hat{X}_i^{α} and \hat{Y}_j^{α} are unitary operators acting on sites i and j , respectively, and $\text{Tr}(\hat{X}_i^{\alpha} \hat{X}_i^{\beta}) = \text{Tr}(\hat{Y}_j^{\alpha} \hat{Y}_j^{\beta}) = \delta_{\alpha\beta}$. We then define $P(\hat{U}) = -\sum_{\alpha} \lambda_{\alpha} \log(\lambda_{\alpha})$. This quantity is closely related to the amount of entanglement the unitary can create between two systems, given additional ancilla systems (assisted entangling power, see e.g. Refs. [40, 41]). For details on the convergence properties of the algorithm, we refer to App. B3.

Emergent geometry of unitary circuits— A powerful way to probe the geometry of the unitary network is to measure the length of “geodesics”, i.e. the shortest paths connecting two physical sites on the boundary of the circuit through the bulk of the circuit (see Fig. 1). The crucial ingredient for a numerical analysis of the unitary circuits is an appropriate notion of length for a path in the circuit that takes into account the strength of each unitary operator. It is obvious that a careful definition of this quantity is necessary: If, for example, one were simply to count the number of unitaries needed to traverse to connect two sites, one would – for a sufficiently deep circuit – always find a length of 1, since eventually all pairs of sites will be directly connected by a unitary. However, deep in the circuit the unitaries are very close to the identity, and therefore do not mediate correlations between the two sites. It is also desirable for the definition of length to be invariant under trivial deformations of the circuit, such as introducing additional swap, identity, or single-qubit gates. Finally, the distance measure should be computable locally and not rely on any global

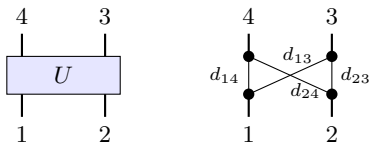


FIG. 2. *Left panel:* Labeling of the input and output indices on a unitary operator. *Right panel:* Local graph corresponding to the unitary operator, with weights labeled on the internal edges. The weight on the edges connecting unitaries is set to 0.

features of the graph.

Our definition of length builds on a local connection between geodesic length and correlations [8]. We construct a weighted, undirected graph as illustrated in Fig. 2: The vertices of the graph are the indices of the unitary operators. Edges connecting different operators have weight 0, while the internal edges connecting different indices of the unitary have lengths d_{ab} as labeled in the right-hand side of Fig. 2. To define d_{ab} , we interpret the unitary as a wavefunction on four qubits and set $d_{ab} = -\log[I(a : b)/(2 \log 2)]$, where $I(a : b)$ is the mutual information between qubits a and b of the normalized wavefunction. Unitarity dictates $d_{12} = d_{34} = \infty$, therefore these two lengths are not included in the graph. Entanglement monogamy [42, 43] implies that if $d_{24} = 0$ ($d_{14} = 0$), d_{13} (d_{23}) must also vanish and d_{14} (d_{24}) must be infinite. Given this weighted, undirected graph, we can compute the minimal distance between two vertices using standard graph theory algorithms.

To develop some intuition for this quantity, we consider the length of a path in well-known tensor networks such as MPS/PEPS and MERA [7]. Assuming that each tensor in such a network has roughly equal strength, we can for now simply take the length to be the number of tensors that a path between two points traverses. In the case of an MPS or PEPS, the length of the geodesic is then simply the physical distance between the sites, indicative of a flat entanglement geometry. In contrast, the length of a geodesic in a MERA scales only logarithmically with the physical distance, since the path is shorter when moving through the bulk of the tensor network [7]; this is a signature of a hyperbolic entanglement geometry.

It is important to emphasize how our definition of geodesic differs from the minimal surfaces in the RT formula for the holographic entanglement entropy (which in 2+1d systems are also geodesics [11]). While our geodesic describes the shortest path to *connect* two sites, the minimal surfaces in the RT formula are anchored at the sites of interest but *separate* the tensor network into two regions. The difference is most easily seen in a matrix-product state: while our geodesics are *linear* in the physical distance, the minimal separating surface is *constant*, since only two bonds (or one, in the case of an open boundary) of the tensor network need to be cut to separate the tensor network. While our definition is more natural in the context of unitary circuits, they are com-

plementary to each other, and both reveal similar information when appropriately interpreted.

It is important to recognize that while our distance measure locally is connected to correlations, there is no simple one-to-one correspondence between the behavior of our geodesics and the behavior of two-point correlation functions. As outlined in Ref. [7], an intuitive relation is for correlations to decay exponentially with the geodesic length. This relation is precise for MPS, and also suggests the possibility of power-law decay of correlations in MERA (although for certain MERA the correlations may decay faster). However, the connection breaks down in the case of a PEPS: while the length of a geodesic is always at least the physical (Manhattan) distance, it is possible to find PEPS whose correlations decay as a power law [44]. Finally, the intricate behavior in a quantum quench discussed below is largely invisible to two-point correlations as they decay exponentially both in the initial localized and final thermal state (albeit controlled by the localization length in the former case, and the thermal length in the latter).

Models— We now turn to the application of our algorithm to candidate wavefunctions of various types. We study the properties of the disentangling circuits in a model of non-interacting spinless fermions in one dimension moving in a disorder potential. We leave the discussion of other models for the appendices (a model for random-singlet type behavior in App. A2 as well as a quasi-disordered model in App. A3). The random-potential model is given by

$$\hat{H} = -t \sum_i \left(\hat{c}_i^\dagger \hat{c}_{i+1} + \hat{c}_{i+1}^\dagger \hat{c}_i \right) + \sum_i w_i \hat{c}_i^\dagger \hat{c}_i, \quad (1)$$

where \hat{c}_i^\dagger creates a spinless fermion on the i 'th site of a chain of length L . Throughout this paper, we work with periodic boundary conditions, set $t = 1$ as an overall energy scale, and focus on Slater determinant states at half filling. The random on-site potential is chosen from a uniform distribution of width W , $w_i \in [-W/2, W/2]$. For vanishing disorder $W \rightarrow 0$, this system is critical and the long-wavelength limit of the ground state is described by a free-boson conformal field theory with central charge $c = 1$. For any finite strength of the disorder potential, the fermions localize [45]. However, for very small $W \ll 1$, the localization length ξ_{loc} is large compared to the system sizes we study, allowing us to break translational invariance without significantly affecting any physically observable properties.

Numerical results— Our numerical findings for the scaling with the physical distance of geodesics in ground states of (1) are shown in Fig. 3 for different disorder strengths. Consider first the case of very large disorder strength, and thus short localization length. The geodesic length initially grows as $d_g \sim \log d_p$ with the physical distance d_p , and then crosses over to a linear dependence $d_g \sim d_p$, indicated by the sharp kink in Fig. 3. This behavior at large physical distance is characteristic

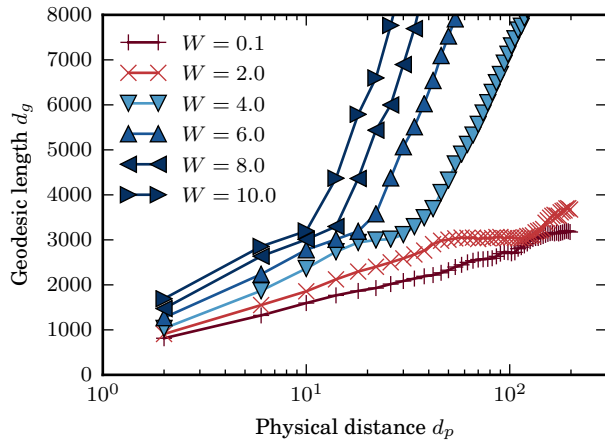


FIG. 3. Geodesic length of the Anderson model at $L = 500$ for different values of the disorder strength W , with 200 realizations each. While the physical distance is given in lattice spacings, the geodesic length is in arbitrary units.

of the flat entanglement geometry expected in a localized state with area-law entanglement. As the disorder strength is decreased, the crossover shifts to larger and larger distances, indicating that the crossover length corresponds to the localization length. The logarithmic dependence thus extends out to larger and larger distances, and ultimately, for very weak disorder potential (such as $W = 0.1$, where the localization length exceeds the system size), spans the entire system. This logarithmic dependence is the hallmark feature of a hyperbolic entanglement geometry and establishes a connection to other holographic mappings, such as the AdS/CFT correspondence.

Going beyond eigenstates, we now consider a quench where the system is initialized in the ground state of (1) with finite disorder ($W = 8$ in the examples chosen here) and thus close to a product state, and is subsequently evolved under the translationally-invariant Hamiltonian ($W = 0$). This is similar to quenching the mass gap from a finite value to zero. We evolve up to time $T = 100$, and perform the disentangling algorithm to obtain $d_g(d_p)$ at various times during the quench. Our results are shown in the left panel of Fig. 4, while the right panel shows the growth of bipartite entropy of a block of ℓ sites, and thus the crossover from area-law to volume-law entanglement entropy scaling. Note that here, in contrast to Fig. 3, the horizontal axis is linear in scale.

Initially, the system exhibits the expected $d_g \sim d_p$ scaling of a localized system. The dominant effect at early times is a fast reduction in the coefficient of this scaling. However, careful examination at early times already reveals a drastic change in the scaling behavior at short distances, where d_g , instead of growing linearly with d_p , becomes nearly constant (or even decreases slightly). There is a sharp kink associated with the crossover from this to the linear behavior, which moves out to larger and larger

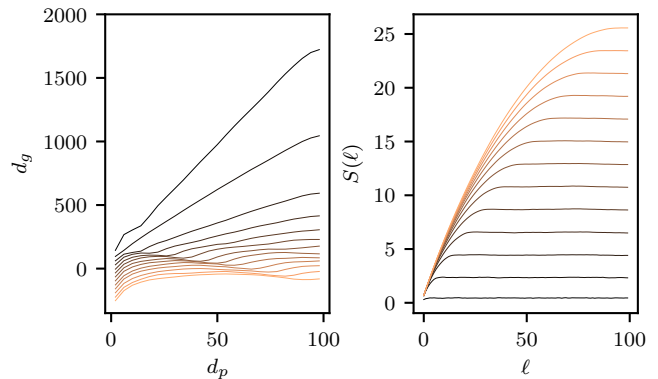


FIG. 4. Quench from the ground state of the Anderson model with $L = 200$ sites and $W = 8$ to the clean case $W = 0$. *Left panel:* Geodesic length d_g as a function of physical distance d_p . *Right panel:* von Neumann entanglement entropy of a contiguous region of ℓ sites. Individual lines represent snapshots of the system at times equally spaced between $T = 0$ to $T = 25.25$ averaged over 200 disorder realizations. Note that the curves in the left panel only have been offset by $-15 \cdot T$. Increasing copper/decreasing blackness indicates times further in the quench.

distances with time, and finally reaches the maximal distance $d_p = L/2$. Comparison with the right panel of Fig. 4 shows that the location of the kink corresponds to the crossover from volume-law to area-law scaling of the bipartite entanglement entropy. Once the system has reached a long-time state with volume-law entanglement entropy, d_g shows some d_p -dependence only for short distances, and is flat otherwise.

In terms of the emergent entanglement geometry, the interpretation of these findings is as follows: the large amount of energy injected into the system at the time of the quench excites a homogeneous and finite density of local excitations, which ballistically spread and entangle with each other. Both the kink and the area- to volume-law crossover follow the spread of this wavefront. For distances beyond this (time-dependent) scale, the unitary circuit is not *qualitatively* affected; however, a *quantitative* change in the coefficient d_g/d_p incurs. Similar to the coefficient of an area law, this is a quantity that is easily changed by a local finite-depth unitary. Within the characteristic length scale, on the other hand, the nature of the circuit is qualitatively changed from a short-ranged circuit encoding an area law state to a very long-ranged circuit, with unitaries connecting the current location of an excitation to its origin, and thus encoding volume-law entanglement. In the final state, this long-ranged unitary circuit dominates the geodesic, with only the short-distance behavior which originates from the boundary of the circuit exhibiting some locality. This bears resemblance to the final state in other holographic theories of quantum quenches [30, 31], with the non-local part of the circuit playing the role of a black hole. The relation of our results for intermediate times to the model put forward in these references is an open question left for future

work. We also note that some details of the emergent geometry, including in particular oscillations observed at times longer than the initial spreading of entanglement shown in Fig. 4, may be due to integrability of the model.

Outlook— While we have so far applied our methods to systems where a holographic description is already known, the fact that we did not make use of any *a priori* knowledge of these systems to extract a holographic structure makes our methods ideally suited to systems where the holographic description is not known. Most prominently, this includes the transition into a many-body localized phase [46–51], which is known to be characterized through entanglement properties [50] while the details of the transition remain controversial [52, 53].

ACKNOWLEDGMENTS

We thank M. P. A. Fisher, G. Refael and J. Sonner for insightful discussions, and A. Antipov and S. Fischetti for comments on earlier drafts of this manuscript.

JRG was supported by the NIST NRC Research Postdoctoral Associateship Award, by the National Science Foundation under Grant No. DMR-14-04230, and by the Caltech Institute of Quantum Information and Matter, an NSF Physics Frontiers Center with support of the Gordon and Betty Moore Foundation.

This material is based upon work supported by the National Science Foundation Graduate Research Fellowship under Grant No. DGE 1144085. Any opinion, findings, and conclusions or recommendations expressed in this material are those of the author(s) and do not necessarily reflect the views of the National Science Foundation.

We acknowledge support from the Center for Scientific Computing at the CNSI and MRL: an NSF MRSEC (DMR-1121053) and NSF CNS-0960316.

This work was in part performed at the Aspen Center for Physics, which is supported by National Science Foundation grant PHY-1066293.

Appendix A: Light cone growth

In a complementary analysis to the geodesics discussed in the main manuscript, we can also characterize the emergent geometry of unitary networks through the growth of light cones. To define the light cone, we interpret the unitary circuit as creating the physical state from an initial product state (i.e., the reverse direction of how it is obtained in the algorithm) and track the effect of changing one of the unitary operators. For an illustration of the light cone in a unitary circuit representing a MERA state, see Fig. 5. It is important to note that a notion of causality is crucial for the definition of a light cone. In the disentangling circuits, this is ensured through the unitarity of each operator. This is a crucial difference to distance discussed in the main

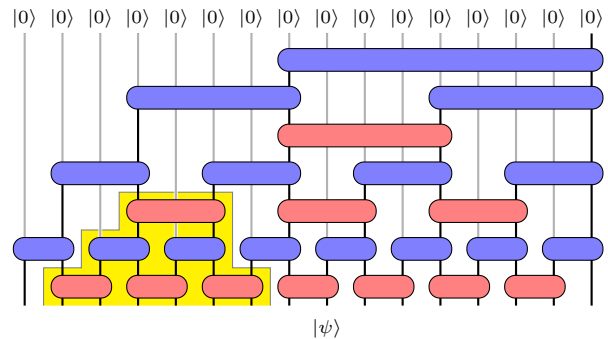


FIG. 5. Two-local unitary network with the structure of a MERA state [25], illustrating the light cone of a bulk operator. To make the structure of the light cone more transparent, the network is interpreted as acting on a product state $|0\rangle^{\otimes L}$ (at the upper end), which is evolved into the physical state $|\psi\rangle$. Each tensor acts only on its ends (thicker lines). The red tensors correspond to disentanglers with two input and two output qubits, while the blue tensors are isometries that take a qubit of an entangled state (thick line) and a previously unentangled qubit (thin line) and entangles them. The circuit’s structure defines a light cone emanating from each unitary in the circuit. Modification of the unitary at the top of the yellow-shaded region will only affect the circuit evolution and physical sites in the region; thus, the yellow region represents a light cone.

manuscript, which could in principle be generalized to non-unitary networks.

We define the width of the light cone emanating from a particular unitary operator as the number of physical sites whose state is affected by changing this unitary operator. Quantifying the depth of the light cone, however, is more subtle. In many ansatz states, such as a scale-invariant MERA, each layer is the same and one can thus simply count the number of layers. However, the operators in the disentangling circuits are all different, and furthermore become closer to the identity as the disentangling procedure progresses and the state approaches a product state. To measure the depth in the circuit, we employ the entangling power $P(\hat{U})$; recall (from the main text) that $P(\hat{U})$ is a measure related to the amount of bipartite entanglement a unitary can create in a multipartite state. We here use the accumulated entangling power of the steps τ up to some step t ,

$$\mathcal{P}(t) = \sum_{\tau < t} P(\hat{U}(\tau)), \quad (\text{A1})$$

where $P(\hat{U}(\tau))$ is the entangling power of the unitary obtained in the τ ’th iteration of the algorithm, to measure the depth into the circuit. We have also explored other measures for the depth, such as the total correlations [54, 55] (see definition below), the average bipartite entropy, and the average mutual information between pairs of sites. For all these quantities, qualitatively similar results are obtained. We restrict our discussion to \mathcal{P} since it has an interpretation purely in terms of the

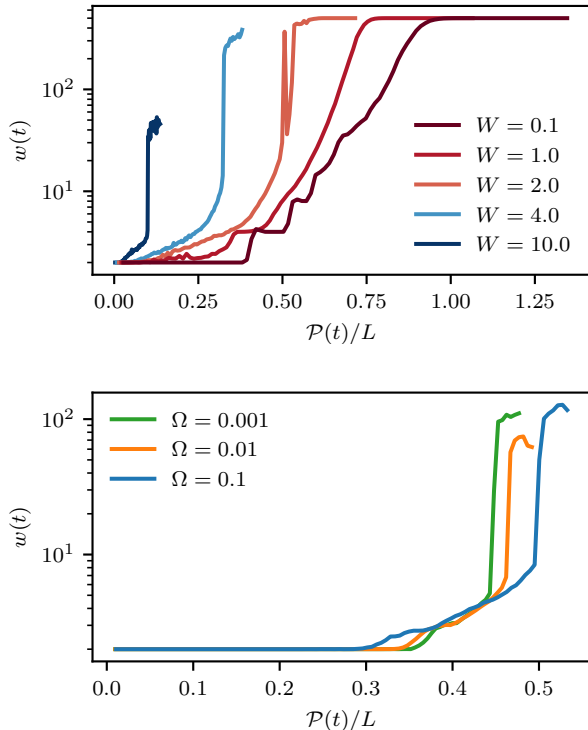


FIG. 6. Width of the light cone $w(t)$. Here, t represents the number of steps into the disentangling circuit. *Top panel:* Ground states of the Anderson model for $L = 500$, for 200 disorder realizations. *Bottom panel:* Ground states in the random-singlet phase for $L = 700$, for 250 disorder realization.

circuit without having to refer to the initial state that the disentangling circuit is applied to.

In a MERA, the width of the light cone grows as $w \sim b^n$, where b is the number of incoming legs on an isometry of the MERA, and n is the number of layers (see Fig. 5). Since the unitaries of a scale-invariant MERA are the same in each layer, the accumulated entangling power is $\mathcal{P} \sim n$, and thus $\log(w) \sim \mathcal{P}$. This reflects the fact that the entanglement of a critical system can be understood as a sum of equal contributions from each length scale [25]. Indeed, since the light cone in a MERA grows as b^n , and the entropy of a region of size l in a critical state follows $\frac{c}{3} \log l$ [37, 56–58], we have that the entropy of a reduced density matrix in a MERA after n layers is $S(\hat{\rho}(n)) \sim \frac{c}{3} \log(b^n) = \frac{nc}{3} \log(b)$ and thus $S(\hat{\rho}(n+1)) - S(\hat{\rho}(n)) = \frac{c}{3} \log(b)$. Each layer of the MERA captures the amount of entanglement encoded at a length scale b^n and makes a constant contribution proportional to the central charge of the system.

Below, we present numerical results for light cone growth as each step of a disentangling unitary circuit is applied. In addition to the Anderson model, we also analyze two further examples: an analogue of a random singlet phase in a chain of free fermions, as well as the André-Aubry model of electrons in a quasi-disordered

potential, which exhibits a delocalized phase even when translational symmetry is broken.

1. Anderson model

Our numerical results for light cone growth in the Anderson model (1) are summarized in Fig. 6. In the top panel, we show results for different strengths of the disorder potential. For $W = 0.1$, the localization length exceeds the system size and the expected scaling behavior for a critical system is observed: after an initial regime where the light cone width remains at $w = 2$, which can be attributed to short-range non-universal physics that is encoded in local correlations, there is a broad regime with the expected scaling of $\log(w) \sim \mathcal{P}$. This regime continues until w saturates to its maximum value. As the disorder strength in the Anderson model is increased and the localization length becomes comparable to the system size, we find that the initial plateau becomes much shorter and the width of the light cone increases very rapidly. This is consistent with the state having a limited amount of short-range entanglement and almost no long-range entanglement.

2. Random singlet phase

The Hamiltonian for the “random singlet phase” is given by

$$\hat{H} = - \sum_i J_i \left(\hat{c}_i^\dagger \hat{c}_{i+1} + \hat{c}_{i+1}^\dagger \hat{c}_i \right), \quad (\text{A2})$$

which we study at half filling. For $J_i = J = 1$, this model coincides with (1) for $W = 0$. However, upon introducing disorder by choosing the J_i randomly and identically distributed, the system flows to a strongly disordered fixed point known as the random singlet phase [34]. At the random-singlet fixed point, the low-energy states take the form of a product of maximally entangled pairs, i.e. for every i there exists another site j such that $I(i : j) = 2 \log 2$ is maximal, while $I(i : k) = 0$ for all $k \neq j$. Despite being very different from the ground states in the clean chain, the entanglement scaling is similar to critical systems with an effective central charge $\tilde{c} = \log 2$ [59].

To obtain the universal behavior of this fixed point in small systems, it is convenient to choose the couplings J_i from the fixed-point distribution,

$$P(J, \Omega) = \frac{\alpha}{\Omega} \left(\frac{\Omega}{J} \right)^{1-\alpha} \Theta(\Omega - J) \quad (\text{A3})$$

where $\alpha = -1/\log \Omega$. The exponent of the distribution is controlled by Ω : for $\Omega = e^{-1} \approx 0.368$, the exponent is 0 and the distribution is a box distribution of width Ω ; for $\Omega \rightarrow 0$, the exponent becomes larger and larger.

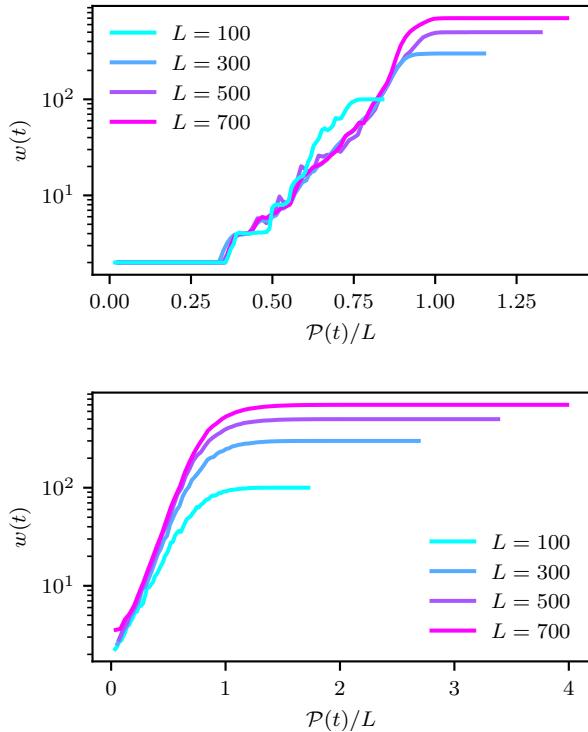


FIG. 7. Light cone growth for the André-Aubry model at $\lambda = 0.1$. *Top panel:* Ground states. *Bottom panel:* Excited states. Note the different scales for the axes in the two plots.

The random-singlet behavior is more pronounced at short scales (high energies) for smaller Ω .

The drastic difference between the structure of the random-singlet states in the lower panel of Fig. 6 and the eigenstates of the Anderson model with small W in the upper panel of Fig. 6 is very apparent in the growth of the light cones. The width of the light cone remains at $w = 2$ for most of the circuit, since most of the entanglement is encoded in two-local (long-ranged) operators. The deviations from this – that is, the point where the light cone grows to $w > 2$ – occur at later times as Ω is reduced, i.e. the system is brought closer to the ideal random-singlet fixed point. As shown in App. B3, the disentangling algorithm also converges drastically faster in the random-singlet phase.

3. André-Aubry model

As a final example, we consider the André-Aubry model [60] given by

$$\hat{H}_{AA} = - \sum_i \left(\hat{c}_i^\dagger \hat{c}_{i+1} + \hat{c}_{i+1}^\dagger c_i \right) + \sum_i \lambda \cos(2\pi qi + \phi) \hat{n}_i, \quad (\text{A4})$$

where \hat{c}_i^\dagger creates a spinless fermion on the i 'th site of a 1d lattice, $\hat{n}_i = \hat{c}_i^\dagger \hat{c}_i$, and we choose $q = (\sqrt{5} + 1)/2$. The model is in a delocalized regime characterized by extended wavefunctions for $\lambda < 2$, while at $\lambda = 2$, the entire spectrum undergoes a localization transition into an Anderson insulator for $\lambda > 2$. Upon adding interactions, the system is known to undergo a many-body localization transition [61]. The fact that extended single-particle wavefunctions can persist even when translational invariance is locally broken by the external potential allows us to at the same time study large systems and obtain smooth results by averaging over different choices of ϕ .

In Fig. 7, we show the growth of light cones in these two cases for a system at half filling. In the case of ground states for small λ , the system exhibits the expected critical scaling $w(t) \sim \exp(\mathcal{P}(t))$ over almost three order of magnitudes in the largest system. In the case of excited states, on the other hand, the width of the light cones diverges very rapidly and saturates to the system size. This indicates that the entanglement is mostly encoded globally in the state.

Appendix B: Details of the disentangling algorithm

1. Optimization of the two-site disentangling unitary

We now describe our strategy for quickly finding a two-site unitary U that maximally reduces the mutual information between two qubits i and j , $I(i : j) = S_i + S_j - S_{ij}$. Since the overall contribution S_{ij} must remain unchanged under unitary transformations, we only need to minimize $S_i + S_j$.

We can write a general unitary rotation on the two-qubit reduced density matrix in the form

$$\hat{U} = |00\rangle\langle 0| + |01\rangle\langle 1| + |10\rangle\langle 2| + |11\rangle\langle 3|, \quad (\text{B1})$$

where $|a\rangle = \{|0\rangle, \dots, |3\rangle\}$ is an orthonormal basis for \mathbb{C}^4 , $\langle a|b\rangle = \delta_{ab}$. Since we can apply a unitary to each qubit without affecting the entanglement properties, we can assume w.l.o.g. that U is chosen such that the reduced density matrices for the two qubits are diagonal,

$$\rho_i = \text{Tr}_j \left(\hat{U} \rho \hat{U}^\dagger \right) = \begin{pmatrix} p_i & 0 \\ 0 & 1 - p_i \end{pmatrix} \quad (\text{B2})$$

$$\rho_j = \text{Tr}_i \left(\hat{U} \rho \hat{U}^\dagger \right) = \begin{pmatrix} p_j & 0 \\ 0 & 1 - p_j \end{pmatrix}, \quad (\text{B3})$$

where

$$p_i = \text{Tr} [\rho(|0\rangle\langle 0| + |1\rangle\langle 1|)] \quad (\text{B4})$$

$$p_j = \text{Tr} [\rho(|0\rangle\langle 0| + |2\rangle\langle 2|)]. \quad (\text{B5})$$

The quantity we want to minimize is then

$$S_a + S_b = H_b(p_i) + H_b(p_j), \quad (\text{B6})$$

where $H_b(p) = -p \log p - (1-p) \log(1-p)$ is the binary entropy.

The strategy we pursue is to choose $|a\rangle$ to be the eigenvectors of ρ , in order of descending eigenvalue. If the eigenvalues of ρ are λ_α , $\lambda_\alpha \geq \lambda_{\alpha+1}$, then $p_i = \lambda_0 + \lambda_1$, and $p_j = \lambda_0 + \lambda_2$. This clearly minimizes S_i , as well as minimizing S_j under the constraint of keeping S_i minimal. While we do not provide a proof that this is the global optimum, further analytical calculation can show that this is a local minimum, and numerical tests have always shown this to be a global minimum.

2. Disentangling algorithm for free fermions

In the case of non-interacting fermions, the entanglement properties of the system are encoded entirely in the correlation matrix (equal-time Green's function)

$$C_{kl} = \langle \hat{c}_k^\dagger \hat{c}_l \rangle, \quad (\text{B7})$$

where \hat{c}_k^\dagger creates a fermion on the k 'th site of the lattice. Given a free-fermion Hamiltonian

$$\hat{H} = \sum_{k,l} h_{kl} \hat{c}_k^\dagger \hat{c}_l = \sum_{\alpha} \epsilon_{\alpha} \hat{d}_{\alpha}^{\dagger} \hat{d}_{\alpha}, \quad (\text{B8})$$

where ϵ_{α} are the single-particle energies and $\hat{d}_{\alpha}^{\dagger} = \sum_i w_{\alpha i} \hat{c}_i^{\dagger}$ creates a fermion in the α 'th eigenstate,

$$C_{kl} = \sum_{\alpha \in F} w_{\alpha k} w_{\alpha l}^*, \quad (\text{B9})$$

where F is the set of filled orbitals.

The entanglement of a group of sites A is obtained by restricting C_{kl} to the sites in A , $C_{kl}^A = C_{kl}$ for $k, l \in A$, computing the eigenvalues λ_{α} of C^A , and then computing $S_A = \sum_{\alpha} H_b(\lambda_{\alpha})$ [37–39], where H_b is again the binary entropy. In particular, for a single site the entropy is simply $S_i = H_b(C_{ii})$.

The mutual information between two sites $I(i:j)$ in a free-fermion state is therefore completely encoded in the 2×2 submatrix of the correlation matrix $C^{\{ij\}}$. Furthermore, if $C^{\{ij\}}$ is diagonal, the mutual information vanishes. To maximally reduce the mutual information, we therefore find the orthogonal rotation $R(\theta)$ of the fermion operators that diagonalizes $C^{\{ij\}}$.

On the many-body operators, this transformation acts according to

$$\hat{c}_i^{\dagger} \mapsto R(\theta)_{11} \hat{c}_i^{\dagger} + R(\theta)_{21} \hat{c}_j^{\dagger} \quad (\text{B10})$$

$$\hat{c}_j^{\dagger} \mapsto R(\theta)_{12} \hat{c}_i^{\dagger} + R(\theta)_{22} \hat{c}_j^{\dagger} \quad (\text{B11})$$

$$\hat{c}_i^{\dagger} \hat{c}_j^{\dagger} \mapsto \det(R(\theta)) \hat{c}_i^{\dagger} \hat{c}_j^{\dagger}. \quad (\text{B12})$$

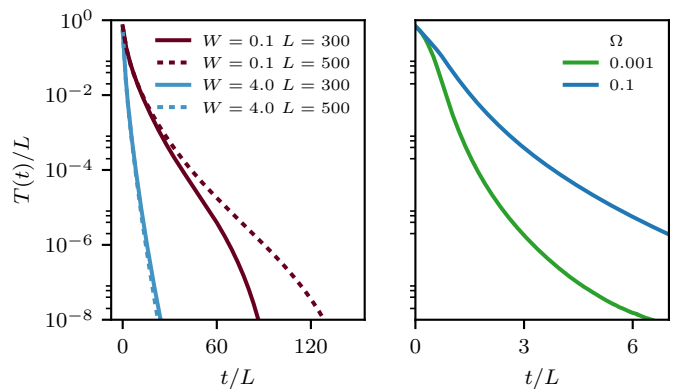


FIG. 8. Convergence of the disentangling algorithm. Here, T denotes the total correlation as given in (B14), and t represents the number of steps into the disentangling circuit. *Left panel:* Ground states of the Anderson model (1). For $W = 0.1$, the localization length exceeds the system size and the system is effectively critical on the length scales considered here, while for $W = 4$ the localization length is smaller than the system size and the effects of localization can be observed. Averaging has been performed over 100 disorder realizations. *Right panel:* Ground states in the random-singlet phase for $L = 700$, averaged over 250 realizations.

This can be succinctly summarized in the block-diagonal matrix

$$U = \left(\begin{array}{c|cc|c} 1 & 0 & 0 & 0 \\ \hline 0 & R(\theta) & & 0 \\ \hline 0 & 0 & 0 & \det(R(\theta)) \end{array} \right), \quad (\text{B13})$$

where care must be taken to correctly implement fermionic anti-commutation rules when applying the off-diagonal elements.

It is interesting to note that for free fermions, the mutual information between two sites can *always* be reduced to zero. While many other entanglement properties of the free-fermion chain are similar to those of weakly interacting fermions in the same phase (for example, the CFT description and thus the universal terms in the entanglement entropy are the same), this is a strong indication of the simpler entanglement structure in non-interacting systems.

3. Convergence

To characterize the convergence of the unitary circuit towards a product state, we measure the distance from a product state [62]. For an easily computable measure of this distance, we rely on the “total correlation” [54, 55], which for a state $\hat{\rho}$ is given by

$$T(\hat{\rho}) = \sum_i S(\hat{\rho}_i) - S(\hat{\rho}), \quad (\text{B14})$$

where $\hat{\rho}_i$ are the reduced density matrices for sites i , and $S(\hat{\rho}) = -\text{Tr} \hat{\rho} \log \hat{\rho}$. The total correlations have the property that $T(\hat{\rho}) = \min_{\hat{\pi}} S(\hat{\rho}||\hat{\pi})$, where $S(\hat{\rho}||\hat{\sigma}) = -\text{Tr}(\hat{\rho} \log \hat{\sigma}) - S(\hat{\rho})$ is the relative entropy, which obeys $S(\hat{\rho}||\hat{\sigma}) \geq |\hat{\sigma} - \hat{\rho}|_1^2/2$, where $|\cdot|_1$ is the trace norm, and $\hat{\pi} = \hat{\pi}_1 \otimes \hat{\pi}_2 \otimes \dots \otimes \hat{\pi}_L$ is the closest product state (in relative entropy) to $\hat{\rho}$. Since we are working over pure states, $S(\hat{\rho}) = 0$ and $T(\hat{\rho})$ is easily computed, since we need to compute the $S(\hat{\rho}_i)$ in the course of the disentangling algorithm. It is worth noting that for pure states $\hat{\rho}$ and $\hat{\sigma}$, $|\hat{\rho} - \hat{\sigma}|_1 = \sqrt{1 - |\langle \hat{\rho} | \hat{\sigma} \rangle|^2}$.

In Fig. 8, we show the convergence of $T(t)/L$ (where $T(t)$ denotes the total correlation of the state after t iterations of the disentangling algorithm) for ground states of the Anderson model as well as the random-singlet model. We consider two disorder strengths for the Anderson model: one which leads to a localization length ξ_{loc} that exceeds the system size, while the other leads to a localization length ξ_{loc} short enough that localization

can be observed for accessible system sizes (L up to 500 sites). In the strongly localized regime, we find very fast convergence that is almost independent of system size. This is expected since localized states obey an area law and are known to be generated by finite-depth local unitaries [50]. In the weakly localized regime, convergence is slower and depends much more on the system size. This is expected since these states violate the area law with a logarithmic correction up to the relevant length scales.

For the random-singlet phase (not shown), we find very rapid convergence to a product state, even though the bipartite entanglement of the initial state is comparable to that of a critical system. This can be explained by the very simple structure of these quantum states, whose entanglement is almost all contained in simple two-site correlations. Convergence is faster for smaller Ω , where the finite-size states are closer to the random-singlet fixed point.

-
- ¹ G. 't Hooft, (1993), [arXiv:gr-qc/9310026](#).
- ² L. Susskind, *Journal of Mathematical Physics* **36**, 6377 (1995).
- ³ J. Maldacena, *International Journal of Theoretical Physics* **38**, 1113 (1999).
- ⁴ E. Witten, *Adv. Theor. Math. Phys.* **2**, 253 (1998), [arXiv:hep-th/9802150](#).
- ⁵ O. Aharony, S. S. Gubser, J. Maldacena, H. Ooguri, and Y. Oz, *Physics Reports* **323**, 183 (2000).
- ⁶ B. Swingle, *Phys. Rev. D* **86**, 065007 (2012).
- ⁷ G. Evenbly and G. Vidal, *Journal of Statistical Physics* **145**, 891 (2011).
- ⁸ X.-L. Qi, Preprint (2013), [arXiv:1309.6282](#).
- ⁹ C. Bény, *New Journal of Physics* **15**, 023020 (2013).
- ¹⁰ A. Mollabashi, M. Naozaki, S. Ryu, and T. Takayanagi, *Journal of High Energy Physics* **2014**, 98 (2014).
- ¹¹ F. Pastawski, B. Yoshida, D. Harlow, and J. Preskill, *Journal of High Energy Physics* **2015**, 1 (2015).
- ¹² N. Bao, C. Cao, S. M. Carroll, A. Chatwin-Davies, N. Hunter-Jones, J. Pollack, and G. N. Remmen, *Physical Review D* **91**, 125036 (2015).
- ¹³ M. Miyaji and T. Takayanagi, *Progress of Theoretical and Experimental Physics* **2015**, 073B03 (2015), [arXiv:1503.03542 \[hep-th\]](#).
- ¹⁴ B. Czech, L. Lamprou, S. McCandlish, and J. Sully, *Journal of High Energy Physics* **2016**, 100 (2016).
- ¹⁵ P. Hayden, S. Nezami, X.-L. Qi, N. Thomas, M. Walter, and Z. Yang, *Journal of High Energy Physics* **2016**, 1 (2016).
- ¹⁶ Z. Yang, P. Hayden, and X.-L. Qi, *Journal of High Energy Physics* **2016**, 1 (2016).
- ¹⁷ S. Kehrein, Preprint (2017), [arXiv:1703.03925](#).
- ¹⁸ X.-L. Qi, Z. Yang, and Y.-Z. You, Preprint (2017), [arXiv:1703.06533](#).
- ¹⁹ M. Fannes, B. Nachtergaele, and R. F. Werner, *Communications in Mathematical Physics* **144**, 443 (1992).
- ²⁰ S. R. White, *Phys. Rev. Lett.* **69**, 2863 (1992).
- ²¹ S. Östlund and S. Rommer, *Phys. Rev. Lett.* **75**, 3537 (1995).
- ²² A. Gendiar, N. Maeshima, and T. Nishino, *Progr. Theor. Phys.* **110**, 691 (2003).
- ²³ T. Nishino, Y. Hieida, K. Okunushi, N. Maeshima, Y. Akutsu, and A. Gendiar, *Progr. Theor. Phys.* **105**, 409 (2001).
- ²⁴ F. Verstraete and J. I. Cirac, Preprint (2004), [arXiv:cond-mat/0407066](#).
- ²⁵ G. Vidal, *Phys. Rev. Lett.* **99**, 220405 (2007).
- ²⁶ G. Vidal, *Phys. Rev. Lett.* **101**, 110501 (2008).
- ²⁷ C. Cao, S. M. Carroll, and S. Michalakis, *Phys. Rev. D* **95**, 024031 (2017), [arXiv:1606.08444 \[hep-th\]](#).
- ²⁸ S. Ryu and T. Takayanagi, *Phys. Rev. Lett.* **96**, 181602 (2006).
- ²⁹ S. Ryu and T. Takayanagi, *Journal of High Energy Physics* **2006**, 045 (2006).
- ³⁰ V. E. Hubeny, M. Rangamani, and T. Takayanagi, *Journal of High Energy Physics* **2007**, 062 (2007).
- ³¹ J. Abajo-Arriastia, J. Aparicio, and E. López, *Journal of High Energy Physics* **2010**, 149 (2010).
- ³² J. Sonner, A. Del Campo, and W. H. Zurek, *Nature Communications* **6**, 7406 (2015), [arXiv:1406.2329 \[hep-th\]](#).
- ³³ S.-K. Ma, C. Dasgupta, and C.-K. Hu, *Phys. Rev. Lett.* **43**, 1434 (1979).
- ³⁴ D. S. Fisher, *Phys. Rev. B* **50**, 3799 (1994).
- ³⁵ C. Chamon, A. Hamma, and E. R. Mucciolo, *Physical review letters* **112**, 240501 (2014).
- ³⁶ Note that while the first iteration is carried out in $\mathcal{O}(L^2 \dim \mathcal{H})$ time, all subsequent iterations can be carried out in $\mathcal{O}(L \dim \mathcal{H})$ time, as only mutual information quantities involving the transformed sites i and j must be recalculated.
- ³⁷ G. Vidal, J. I. Latorre, E. Rico, and A. Kitaev, *Phys. Rev. Lett.* **90**, 227902 (2003).
- ³⁸ I. Peschel, *Journal of Physics A: Mathematical and General* **36**, L205 (2003).
- ³⁹ I. Peschel and V. Eisler, *Journal of Physics A: Mathematical and Theoretical* **42**, 504003 (2009).
- ⁴⁰ P. Zanardi, *Phys. Rev. A* **63**, 040304 (2001).
- ⁴¹ X. Wang, B. C. Sanders, and D. W. Berry, *Phys. Rev. A*

- [67](#), [042323](#) (2003).
- ⁴² V. Coffman, J. Kundu, and W. K. Wootters, *Phys. Rev. A* **61**, [052306](#) (2000).
- ⁴³ B. M. Terhal, IBM Journal of Research and Development **48**, 71 (2004).
- ⁴⁴ F. Verstraete, M. M. Wolf, D. Perez-Garcia, and J. I. Cirac, *Phys. Rev. Lett.* **96**, [220601](#) (2006).
- ⁴⁵ P. W. Anderson, *Phys. Rev.* **109**, 1492 (1958).
- ⁴⁶ D. M. Basko, I. L. Aleiner, and B. L. Altshuler, *Annals of Physics* **321**, [1126](#) (2006).
- ⁴⁷ V. Oganesyan and D. A. Huse, *Phys. Rev. B* **75**, [155111](#) (2007).
- ⁴⁸ A. Pal and D. A. Huse, *Phys. Rev. B* **82**, [174411](#) (2010).
- ⁴⁹ J. H. Bardarson, F. Pollmann, and J. E. Moore, *Phys. Rev. Lett.* **109**, [017202](#) (2012).
- ⁵⁰ B. Bauer and C. Nayak, *J. Stat. Mech: Theor. Exp.* **9**, [09005](#) (2013), [arXiv:1306.5753](#) [cond-mat.dis-nn].
- ⁵¹ D. J. Luitz, N. Laflorencie, and F. Alet, *Phys. Rev. B* **91**, [081103](#) (2015).
- ⁵² T. Grover, Preprint (2014), [arXiv:1405.1471](#).
- ⁵³ V. Khemani, S. P. Lim, D. N. Sheng, and D. A. Huse, Preprint (2016), [arXiv:1607.05756](#).
- ⁵⁴ K. Modi, T. Paterek, W. Son, V. Vedral, and M. Williamson, *Phys. Rev. Lett.* **104**, [080501](#) (2010).
- ⁵⁵ K. Modi, A. Brodutch, H. Cable, T. Paterek, and V. Vedral, *Rev. Mod. Phys.* **84**, [1655](#) (2012).
- ⁵⁶ M. Srednicki, *Phys. Rev. Lett.* **71**, [666](#) (1993).
- ⁵⁷ C. Callan and F. Wilczek, *Physics Letters B* **333**, [55](#) (1994).
- ⁵⁸ C. Holzhey, F. Larsen, and F. Wilczek, *Nuclear Physics B* **424**, [443](#) (1994).
- ⁵⁹ G. Refael and J. E. Moore, *Phys. Rev. Lett.* **93**, [260602](#) (2004).
- ⁶⁰ S. Aubry and G. André, *Ann. Israel Phys. Soc* **3**, 18 (1980).
- ⁶¹ S. Iyer, V. Oganesyan, G. Refael, and D. A. Huse, *Phys. Rev. B* **87**, [134202](#) (2013).
- ⁶² V. Vedral, M. B. Plenio, M. A. Rippin, and P. L. Knight, *Phys. Rev. Lett.* **78**, [2275](#) (1997).